Enhancing the Thermosiphon-Driven Discharge of a Latent Heat Thermal Storage System used in a Personal Cooling Device

ROHIT DHUMANE[a], ANNE MALLOW[b], YIYUAN QIAO[a], KYLE R. GLUESENKAMP[b], SAMUEL GRAHAM[b,c], JIAZHEN LING[a*], REINHARD RADERMACHER[a]

[a] *Center for Environmental Energy Engineering, University of Maryland, College Park, MD, USA*
[b] *Oak Ridge National Laboratory, Oak Ridge, TN, USA*
[c] *Georgia Institute of Technology, Atlanta, GA, USA*

Personal cooling devices reduce energy loads by allowing buildings to operate with elevated setpoint temperatures, without compromising on the occupant comfort. One such novel technology called the Roving Comforter (RoCo) uses a compact R134a based vapor compression system for cooling. Following its cooling operation, during which waste heat from the condensing refrigerant is stored in a phase change material (PCM), a two-phase loop thermosiphon is used to discharge (solidify) the PCM to enable its next operation. The transient operation of this thermosiphon is the focus of the present article. Use of a PCM as the storage medium provides high energy density due to the ability to store thermal energy as latent heat during the phase transition; however, the discharge rate is limited by the low thermal conductivity of the PCM. Insertion of a graphite foam within the PCM can increase the rate of discharge and decrease the downtime of the cooling device. Since graphite enhancement involves a tradeoff between improving the discharge time at the expense of PCM volumetric latent heat, the impact of graphite foam density on the PCM discharge rate is investigated by using a Modelica-based transient model of the thermosiphon. The semi-empirical model, which uses relevant heat transfer coefficient and pressure drop correlations for both refrigerant and airside heat transfer, captures the complex phenomena involving simultaneous phase change of the refrigerant and the PCM. The graphite enhanced PCM selected from this analysis results in a 51% reduction in the discharge time with addition of only 5% to the thermal storage weight, without compromising the required cooling time.

Keywords: Phase change material; Thermosiphon; Thermosyphon; Modelica; Two-phase

*Corresponding author. Email address: jiazhen@umd.edu

1. **Introduction**

The building sector accounts for about 41% of the primary energy consumption in the United States, with space heating and cooling taking up 21.5% and 11.8% of that fraction, respectively [1]. Personal conditioning systems (PCS) have dual benefits of saving energy and providing improved thermal comfort. Some of the typical strategies used in providing localized thermal comfort may involve a combination or individual use of the technologies listed below:

- Personalized ventilation and body local air jets [2]–[6]: These typically include strategies like personal fans, nozzle guided airflows, and a combination of ventilated air with conditioned air to provide comfort to a sedentary occupant in workspace environment. Recently, researchers have reported on integration in bedrooms [7].
- Footwarmers, legwarmers, radiant panels [8]–[10]: Radiant cooling and/or heating can also be integrated with workspace to provide comfort.
- Comfort chairs (heated, cooled and/or ventilated) [11]–[13]: Thermo-electric devices or fans may be incorporated to provide comfort to the seated occupant.
- Personal comfort garments [14]–[17]: These are typically used in specialty fields like military training, firefighting, medical operation, office workers and sports.
- Evaporative coolers [18]–[21]: These have proven to be advantageous in hot and dry climate. They involve evaporation of water to provide both cooling and humidification.

Dhumane et al. [22] introduced a novel concept of portable PCS to mitigate the challenges faced by current PCS including high retrofit costs, limited regions of comfort near installation, and addition to building energy loads, which have limited their market potential. Heidarinejad et al. [23] demonstrated the potential savings of energy, cost, and CO_2 emissions from commerical buildings in different U.S. cities from this technology. The technology is suitable for midrise apartments and offices which have full time employees or residents, rather than a large population of transient occupants such as in retail buildings [23]. Zhu et al. [24] studied the cooling efficiency for this type of technology by changing nozzle diameters and supply air velocity for both seated and standing occupants. They found that forced convection generated by the air flow rate from the nozzle leads to the sensible heat removal from the occupant. They recommended that the device

cooling capacity should target the increase in airflow rate instead of cooling personalized air for improved energy efficiency.

The present article provides operational details of a vapor compression cycle based portable personal cooling system and focuses on its discharge operation. This system uses a latent heat thermal storage system to store condenser heat, which needs to be discharged after it is saturated. A thermosiphon is used for this discharge process.

The two-phase closed loop thermosiphon is a gravity-assisted natural convection flow loop, in which heat is transferred as the latent heat of a working fluid between the heat source and heat sink. Thermosiphons can operate with relatively small temperature differences and without any moving parts, making them ideal for operations where low cost, energy efficiency, less noise and reliability are important. Consequently, they have several applications in electronics cooling [25], solar energy conversion systems [26], [27], telecommunication devices [28], [29], and load reduction in buildings [30]. The present work focuses on modeling a thermosiphon used to discharge a phase change material (PCM) integrated into a heat exchanger (PCM-HX) of an innovative portable personal cooling device called the Roving Comforter (RoCo) [31]. By providing localized cooling, RoCo enables elevation of building setpoint temperatures up to 2.2°C. This reduction in building cooling load can lead to energy savings in the range of 10-30% depending on the location [32].

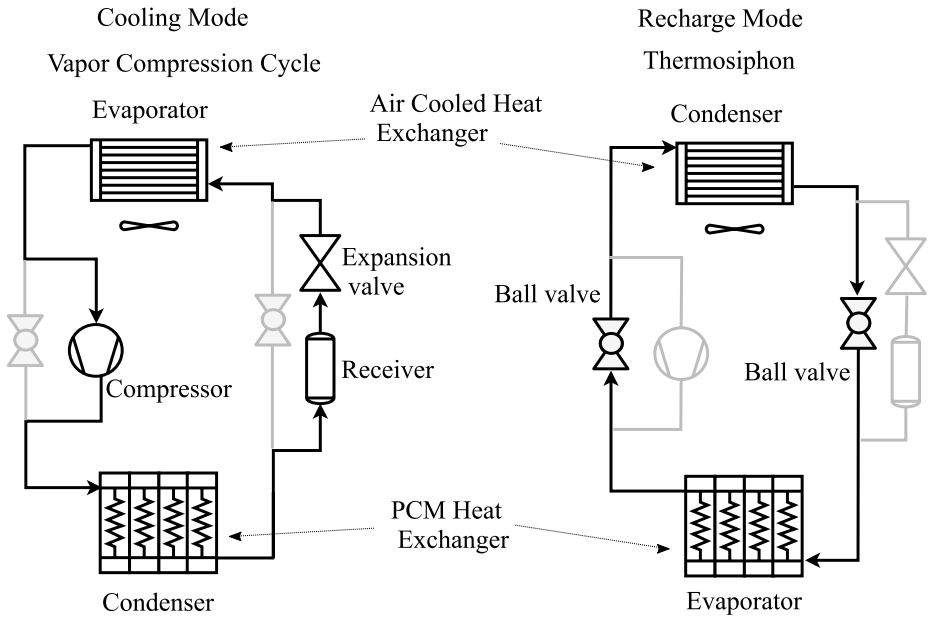

Figure 1: Schematic for vapor compression (left) and thermosiphon (right) modes of operation (gray portion of the refrigerant circuit is inactive in the particular mode).

The two alternating operating modes of RoCo are shown in Figure 1. The cooling operation (Figure 1, left) is reliant on an R134a based vapor compression cycle (VCC). Heat removed from the condensing refrigerant during the VCC operation is captured by a commercial, paraffin-based PCM (PureTemp 37, T_{melt} = 37°C, k = 0.2 $Wm^{-1}K^{-1}$ [33]) surrounding the condenser refrigerant tubing to avoid an addition to the building heat load. This PCM was chosen since the phase transition temperature enables high COP in the VCC operation due to the low melting temperature, but does not liquify by heat transfer with the surroundings since the transition temperature is 9°C higher than the weighted mean of the US summer dry bulb temperature [34]. Stability of this material has been demonstrated over 65,000 thermal cycles [33].

The cooling operation terminates when the PCM is completely melted since the condenser can no longer store rejected heat from the refrigerant as latent energy, leading to elevated condenser temperatures and decreased cycle efficiency. Thus, there is a need for re-solidification of the PCM (PCM discharge) before the next cooling operation. Since the PCM is insulated from the ambient to minimize heat loss to the conditioned space during cooling, a thermosiphon operation in the same refrigerant circuitry is employed to enable a controlled discharge process.

In the thermosiphon operation, liquid refrigerant in the PCM-HX absorbs heat from the PCM and vaporizes. The thermosiphon operation is used to discharge the heat stored during the cooling operation. Typically, the cooling is required during the day time and thermosiphon is at night time. This also facilitates peak load shifting from the electricity grid as the discharge is done during the off-peak hours and provides cost savings to customers. There are two methods to reject the heat during night time: (1) reject heat to the internal spaces during the night when the building is unoccupied and the building load is insignificant (2) reject heat outside the conditioned space by moving the RoCo[23]. The vapor rises and condenses in the air-cooled heat exchanger (AC-HX). The condensed liquid flows back by gravity to the PCM-HX. A receiver is included in the circuit to ensure that the PCM-HX is filled with liquid refrigerant to prevent dry out during the thermosiphon operation. The initial PCM-HX prototype provided 2 hours of cooling operation and required 8 hours for discharge [31], limiting RoCo to a single cooling operation per day. The long discharge time can be attributed to the low thermal conductivity of the PCM.

One method to increase the thermal conductivity is to create a composite with PCM and a highly conductive porous compressed expanded natural graphite (CENG) foam [35]–[37]. The saturation of CENG foams with PCM has been shown to increase the thermal conductivity by more than an order of magnitude; however, this reduces the latent heat storage of the PCM up to 35% due to the displacement of PCM by graphite as well as air contained within closed pores formed during the fabrication process[35]–[37]. The reduced latent heat of the PCM leads to increased weight and volume of the composite, which is not desirable for a portable device like RoCo. Thus, there is a tradeoff between the reduced discharge time and increased volume in the material selection. A transient analysis of the thermosiphon mechanism is carried out to determine the optimum graphite bulk density of the PCM composites developed by Mallow et al.[38].

2. Literature Review of Thermosiphon Modeling

The development of predictive tools for heat pipe technologies, such as a thermosiphon, remains an active field of research. Dobran [39] and Reed and Tien [40] were the first to study comprehensive control volume (CV) based models for counter-current thermosiphons. Examples of counter-current thermosiphon analysis are discussed in review articles [41]–[43].

Industrial applications typically involve co-current two-phase loop thermosiphons (TPLT) due to their capability of transporting large heat quantities and less liquid-vapor interaction [44]. Several steady-state models are available in the literature for TPLT [25], [30], [45]–[47] developed using commercial software such as Engineering Equation Solver® [48] and MATLAB® [49]. However, solidification of PCM is inherently a transient phenomena, so these models are inapplicable for modeling the RoCo operation. Transient models for TPLT are scarce in the literature. The first model for TPLT based on the CV approach for performance in transient operation was developed by Vincent and Kok[44]. This model requires saturation temperature of the evaporator during its steady-state operation as an input and provides transient behavior for perturbations of a thermosiphon from that steady-state condition. A fully explicit distributed parameter model was developed by Dobson and Ruppersberg [50] for transient modeling and validation of a thermosiphon used for cooling the concrete containment structure surrounding a nuclear reactor. Most recently, a transient one-dimensional flow model for TPLT considering a two-phase mixture in both mechanical and thermal equilibrium was developed by Bodjona et al.[51]. This two-phase flow model can describe various states of refrigerant and compute phase transitions. However, validation of the model is not presented, and the applicability of the model to a practical setup requires additional study. Furthermore, these models [50], [51] use transient profiles for the heat input, limiting analysis only to the refrigerant side. Integration of a PCM within a heat pipe is modeled by Srikanth et al.[52] using CFD. However, this framework is not suitable to capture variation in refrigerant properties.

This work presents a semi-empirical model for a thermosiphon with transient equations not only for the refrigerant side but also the thermal storage. The state of the PCM is part of the solution, adding further to the complexity of the model. Modelica® [53] is used for modeling because of the object-oriented, declarative, and acausal modeling approach, reusable libraries for two-phase flow, refrigerant media property packages[54] based on REFPROP® 9.0 database and differential algebraic equation solvers. This enables development of the model with similar detailing on the refrigerant side as Bodjona et al.[51], without the need to write equations for refrigerant properties and solvers. To the authors' knowledge, this is the first demonstration of modeling a two-phase thermosiphon using this language, which is increasingly being used for dynamic modeling of complex physical systems, and so implementation details are included.

Additionally, a numerical model with PCM integrated with TPLT has not been found in the literature, and the current article highlights challenges in modeling the underlying physics.

3. Component Modeling

This section discusses equations and assumptions used in the component models for the thermosiphon system model. The component models will be combined to form the system model, which will be first validated with experimental data and then used to evaluate the thermal storage performance of graphite enhanced PCM.

3.1. Downcomer and Riser

The connecting tubes between the evaporator and condenser act as the downcomer and riser. Their dynamics is expected to be on a timescale faster than those of the heat exchangers. One of the important simplifications in the modeling of dynamic systems is the time scale abstraction in which faster timescales are treated as a steady state. The mass and energy storage in these components is hence neglected based on this assumption. The momentum equation is used to evaluate the mass flow rate in the system. Such components are referred to as flow models in Modelica terminology. The finite volume discretization of the momentum equation for such components is described in Elmqvist et al.[55]. For the lumped control volume of the downcomer (Figure 2), equating mass flow rates at the inlet and outlet leads to Equation 1.

$$\frac{d\dot{m}}{dt}L = A(p_{in} - p_{out}) - \frac{1}{2}\frac{\dot{m}^2}{\rho A^2} fSL - A\rho g\Delta z \tag{1}$$

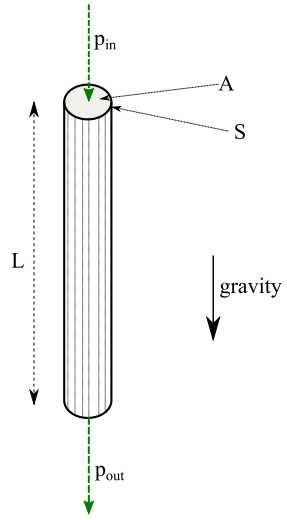

Figure 2: Control volume for downcomer.

Based on inlet and outlet heights, Δz=-L for the downcomer and Δz=L for the riser. The friction factor, *f*, is calculated using spline interpolation between Hagen-Poiseulle (Equation 2) and Blasius (Equation 3) [56] equations to account for both laminar and turbulent flows for single-phase refrigerant as shown below in Equations 4 and 5. The modeling assumes a single phase flow in both the downcomer and riser. The objective of the current investigation is the heat transfer characteristics of the thermosiphon for which the assumption is valid (the sensible heat of R134a is very small compared to its latent heat). However, for an investigation focused on fluid flow characteristics, it may be necessary to develop a more detailed model for the downcomer and riser. Interpolation is necessary to avoid chattering issues encountered in transient simulations with equations that are not continuous and differentiable. Figure 3 shows the interpolated equation (Equation 5) in comparison with the two correlations.

$$f_1 = \frac{64}{\mathrm{Re}} \tag{2}$$

$$f_2 = \frac{0.315}{\mathrm{Re}^{0.25}} \tag{3}$$

$$y = \begin{cases} 0, & \text{if } \left(\frac{3000 - \mathrm{Re}}{1000}\right) < -1 \\ 1, & \text{else if } \left(\frac{3000 - \mathrm{Re}}{1000}\right) > 1 \\ 0.5 \tanh\left(\tan\left(\frac{\pi}{2}\left(\frac{3000 - \mathrm{Re}}{1000}\right)\right)\right) + 1, & \text{else} \end{cases} \tag{4}$$

$$f = y f_1 + (1 - y) f_2 \tag{5}$$

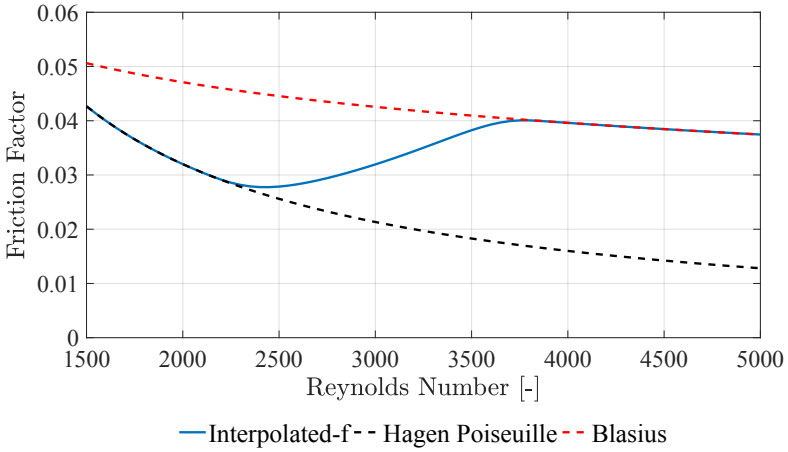

Figure 3: Friction factor function used in the riser and downcomer.

3.2. Thermosiphon Condenser

The fin and tube AC-HX component, or thermosiphon condenser, is modeled using a segment-by-segment heat exchanger model (see Figure 4), which consists of three sections: the refrigerant flow (green), finned walls (orange), and air stream (blue). Each of these sections is linked via heatports and fluidports, which are the standard connectors for thermo-fluid components in the Modelica Standard Library. A detailed discussion of this component is presented in Qiao et al.[57], and only a short explanation is provided here for brevity.

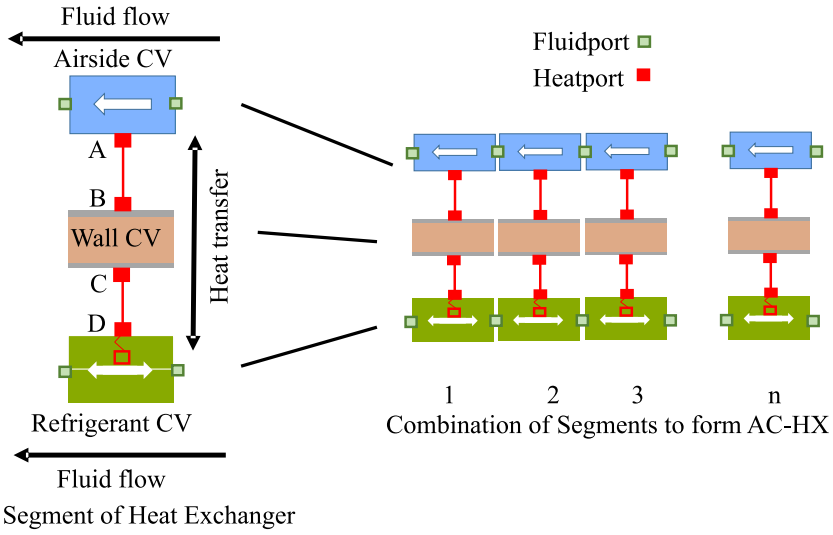

Figure 4: Arrangement of control volumes to model AC-HX.

The heat transfer between the refrigerant tube walls and fins is calculated using the lumped capacitance method and is shown by the energy equation in Equation 6. The axial conduction along the tube is neglected. T_{tube} is the temperature at a node halfway along the thickness (Δd) of the refrigerant tube.

$$\left(m_{tube}c_{tube} + m_{fin}c_{fin}\right)\frac{dT_{tube}}{dt} = \dot{Q}_r + \dot{Q}_a \tag{6}$$

The locations of heatports A, B, C, and D are shown in Figure 4; connected heatports have the same temperature ($T_A = T_B$; $T_C = T_D$). heatports B and C are used to evaluate the heat transfer within the refrigerant tubing control volume, while heatports A and D are used for the airside control volume and refrigerant control volume, respectively. The thickness of the refrigerant tube is much smaller than its diameter, enabling evaluation of wall conduction by Equations 7 and 8 for the airside ($\dot{Q}_a$) and the refrigerant side ($\dot{Q}_r$).

$$\dot{Q}_r = \frac{kA}{\left(\Delta d/2\right)}\left(T_C - T_{tube}\right) \tag{7}$$

$$\dot{Q}_a = \frac{kA}{\left(\Delta d/2\right)}\left(T_{tube} - T_B\right) \tag{8}$$

The airside and refrigerant side cooling capacities are evaluated in their respective control volumes using Equations 9 and 10. By connecting the fluidport and heatport interfaces for the component blocks (Figure 4), any complex circuitry can be represented by this model.

$$\dot{Q}_a = -\dot{m}_a \left[c_{p,a} \left(T_{a,in} - T_{a,out} \right) + \left(\omega_{a,in} - \omega_{a,out} \right) h_{fg} \right] \tag{9}$$

$$\dot{Q}_r = \alpha_r A \left(T_D - T_r \right) \tag{10}$$

The outlet state of the air temperature is evaluated using ε-NTU approach (Equation 11), and the humidity ratio is evaluated by the Lewis analogy (Equation 12). By applying Hong and Webb equation [58] for fin efficiency, the tube walls and fins are lumped together using one temperature to calculate the effective airside heat transfer area (A_{eff}) used in Equations 11 and 12. Calculation of α_r and α_a will be discussed in the system modeling section. The refrigerant side contains transient conservation equations, which are evaluated with pressure and enthalpy as state variables. A detailed discussion of these equations and their derivations is presented in Qiao et al.[57].

$$T_{a,out} = T_{a,in} + \left(T_A - T_{a,in} \right) \left(1 - e^{\left(\frac{-\alpha_a A_{eff}}{\dot{m}_a c_{p,a}} \right)} \right) \tag{11}$$

$$\omega_{out} = \omega_{in} + \min\left(0, \omega_A - \omega_{in} \right) \left(1 - e^{\left(\frac{-\alpha_a A_{eff}}{\dot{m}_a c_{p,a} Le^{2/3}} \right)} \right) \tag{12}$$

3.3. Phase Change Material Control Volumes

Several models exist in the literature for modeling the melting and solidification of PCM [59]–[61]. The enthalpy method [62] is used in the current study due to the advantage of carrying out calculations on a fixed grid with an implicit treatment of the phase change boundary.

The energy equation applied to the PCM control volume gives rise to Equation 13. The PCM-HX involves helical tubes surrounded by PCM, which results in very complicated 3D mathematical equations involving phase change and refrigerant flow. For the purpose of current research, two primary assumptions are made to obtain equations for system level simulation. First, the PCM control volume is modeled as a lumped system. This eliminates the need for 3D momentum equations for natural convection flow within the molten PCM. Secondly, since the density difference between the solid and liquid phase of PCM is less than 10%, the average value of densities of both the phases is used in the calculations. These two assumptions enable modeling a simpler form of the energy equation shown in Equation 14.

$$\rho \frac{\partial h}{\partial t} + \nabla(\rho u h) = \nabla k (\nabla T) \tag{13}$$

$$m_{pcm}\frac{dh}{dt} = \dot{Q}_{pcm} \tag{14}$$

The PCM modeling consists of two components: one to model its heat storage and a second to model its rate of heat transfer.

3.3.1. PCM Heat Storage

The PCM heat storage is modeled using a component named PCM Capacitor. It models the left-hand side of Equation 14. The only unknown variable in the enthalpy method formulation is the enthalpy-temperature dependency of the PCM which is calculated using Equation 15. The PCM solidifies over the temperature range from T_L to T_S. DSC measurements were taken using a TA Instruments Q2000 with a heating and cooling speed of 5°Cmin^{-1} to obtain the variations of the effective specific heat capacity, c(T), in the interface region. The point where the PCM just starts to melt is taken as the zero reference for the enthalpy function.

$$h(T) = \begin{cases} -\int_{T_s}^{T} c_s \cdot dT & \text{(solid)} \quad T < T_s \\ \int_{T_s}^{T_l} c(T) \cdot dT & \text{(interface)} \quad T_s < T < T_l \\ h_{sl} + \int_{T_l}^{T} c_l \cdot dT & \text{(liquid)} \quad T_l < T \end{cases} \tag{15}$$

3.3.2. PCM Heat Transfer

The heat transfer from the PCM is modeled using the PCM Conductor block. To enable modeling of any heat exchanger geometry, either with a helical or straight refrigerant tube, the heat transfer coefficient as a function of melt fraction, λ, is set as an input and evaluated by experimental or numerical methods. This enables modeling varying effects of conduction and natural convection, which occurs in the case of a non-enhanced PCM with helical refrigerant tubes. The conduction dominant heat transfer in a graphite enhanced PCM with straight refrigerant tubes can also be captured using the same component.

The melt fraction is calculated from PCM enthalpy by using Equation 16 in the PCM Capacitor block. It is then provided as an input to the PCM Conductor block. The use of the heat transfer coefficient, α_{pcm}, simplifies the right-hand side of Equation 14 as shown in Equation 17. Calculation of α_{pcm} will be discussed in the subsection 3.3.3 for the case of pure PCM and in section 5 for the graphite enhanced PCM. The net

value of net heat transfer is calculated using the temperature difference between PCM Conductor and lumped refrigerant CV (Equation 17).

$$\lambda = \min\left(1, \max\left(0, \frac{h}{h_{sl}}\right)\right) \tag{16}$$

$$\dot{Q}_{pcm} = \alpha_{pcm} A (T_{tube} - T_{pcm}) \tag{17}$$

3.3.3. Empirical heat transfer coefficient function

The empirical heat transfer coefficient as a function of melt fraction, which is an input for the PCM Conductor (Equation 17), is not available in the literature and is, hence, obtained by an experiment. The heat transfer coefficient evaluation procedure is similar to the one adopted by Merlin et al. [63] and is only briefly explained for the sake of brevity. The experimental setup (see Figure 5, left image) includes a single helical coil (see Figure 5, right image) placed inside a cylinder filled with PCM. It is representative of one quarter of the PCM-HX. A peristaltic pump is used to circulate water through a PID-controlled heater to melt the PCM at a constant water inlet temperature. During solidification, the heater is turned off. The pump continues to circulate water through the circuit during solidification. An air to water heat exchanger cools the water temperature at the inlet to a constant value. This value can be adjusted by changing the temperature of the environmental chamber where the setup is placed. The entire PCM-HX is insulated with foam to minimize heat losses to the surroundings.

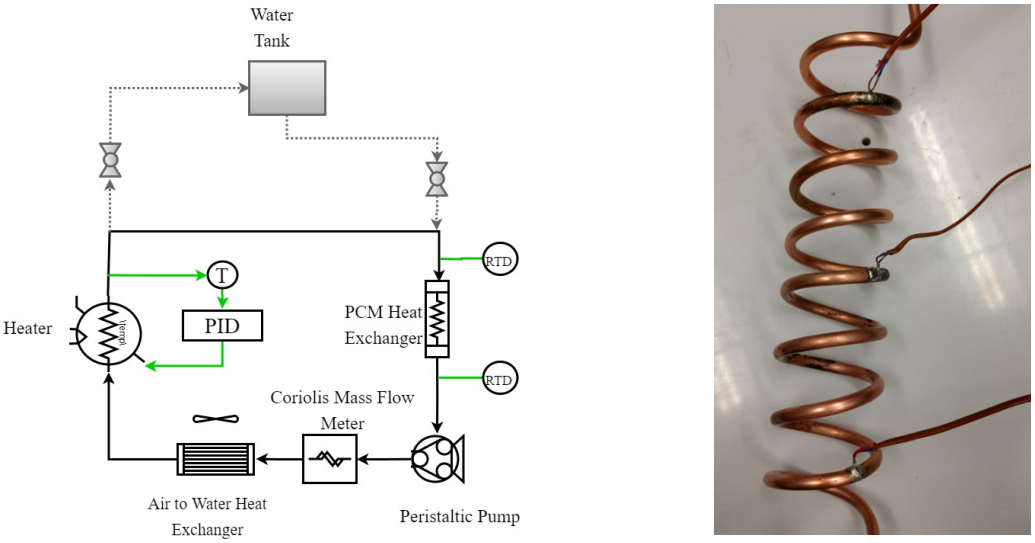

Figure 5: Schematic of the experiment setup used to obtain empirical heat transfer coefficient function (left), Helical coil used for the experiment (right)

The instrumentation used for the evaluation of the heat transfer coefficient is summarized in the Table 1. The experiment is repeated three times to ensure repeatability of the data. The standard deviation in the RTD measurements is 0.04°C. The uncertainty associated with the heat transfer coefficient is estimated to be 13%, when the temperature difference between the RTD values is 1.2°C. Three thermocouples are soldered to the helical coil to measure the helical coil temperature, while ten thermocouples are evenly distributed inside the PCM. The average values of these thermocouples provide the tube temperature and lumped PCM temperature used in the determination of the heat transfer coefficient.

Table 1: Summary of measurement devices

Manufacturer	Device	Accuracy Range	Accuracy Specification
Omega Engineering Inc.	RTD (Ultra Precise 1/10 DIN)	0 to 100°C	±1/10 (0.3 + 0.005 |t|)°C From 0 to 100°C
Omega Engineering Inc.	T-type thermocouple	-200 to 350°C	±0.5°C
Emerson	Micro Motion Coriolis flow meter	0-100 $g.s^{-1}$	0.2% of the flow rate

The results of temperatures measured in the experiment are shown in the Figure 6. The flow rate of water is constant during the experiment. Mean value of this water flow rate is 3.11 $g.s^{-1}$ with a standard deviation of 0.03 $g.s^{-1}$.

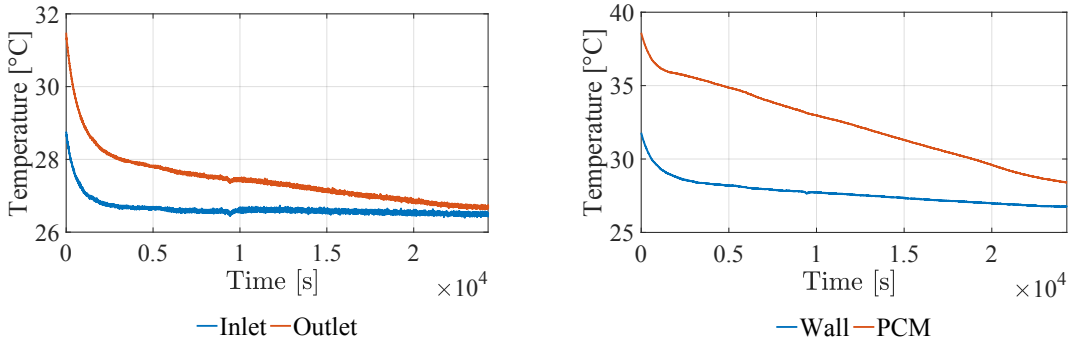

Figure 6: Temperatures measured by RTD's (resistance temperature detector) located on the water-side at inlet and outlet of PCM-HX (left), Temperatures averaged from the three thermocouples for wall, and ten thermocouples located inside PCM (right)

The net heat transfer from the PCM to the water is evaluated by Equation 18. The temperatures at the inlet and outlet are both provided by the RTD's. The averaged values of the temperatures from Figure 6

(right) are used to evaluate the heat transfer coefficient. Equations 15-16 are used to obtain melt fraction as a monotonic function of the lumped PCM temperature (see Figure 7, left).

$$\dot{Q} = \dot{m} c \left(T_{out} - T_{in} \right) \tag{18}$$

$$\dot{Q} = \alpha A \left(T_{tube} - T_{pcm} \right) \tag{19}$$

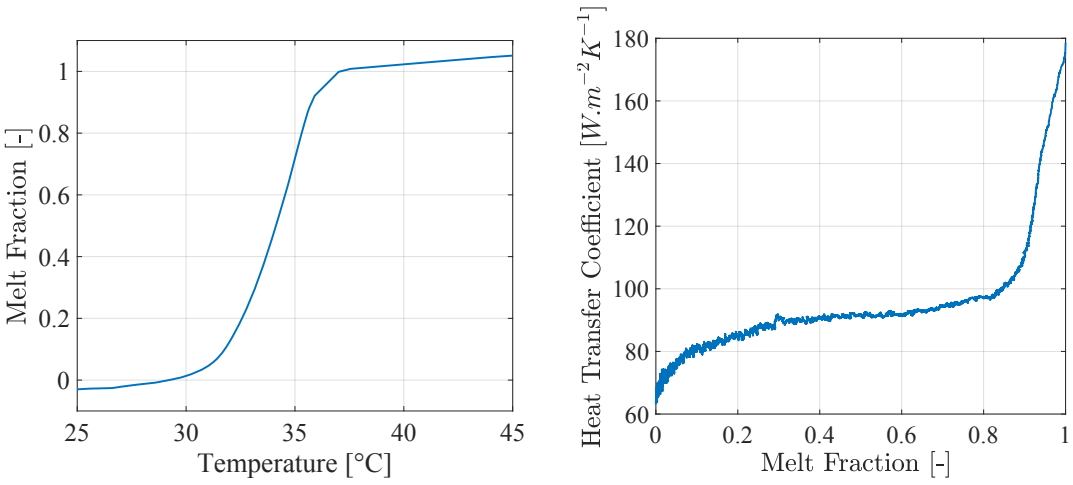

Figure 7: Melt fraction as a function of temperature (left), Heat transfer coefficient as a function of melt fraction (right)

Finally, the empirical relationship between the heat transfer coefficient and melt fraction is obtained (Figure 7, right). The profile shows that the heat transfer rate decreases as the PCM solidifies from liquid (melt fraction = 1) to solid (melt fraction = 0). This can be attributed to the decrease in temperature accompanying the phase change, also known as the temperature glide. As the PCM solidifies, its temperature decreases. As a result, the water entering the PCM-HX at a fixed temperature has less heat transferred to it.

3.4. Thermosiphon Evaporator Control Volume

The state of refrigerant leaving the PCM-HX is assumed to be saturated vapor since it is a TPTL. After the liquid levels are balanced in the downcomer and riser tubes, the mass flow rate of the thermosiphon depends on the rate of evaporation from the PCM-HX. The mass flow rate in the circuit is calculated from the rate of evaporation of the refrigerant from the PCM-HX. Nominal values of pressure drops are added to various component models to obtain a mass flow rate comparable to the value calculated by back calculation from the airside data. This is done because the mass flow meter is bypassed in the experimental setup to

reduce the pressure head for the refrigerant flow in the thermosiphon operation. Since no experimental measurement of mass flow rate is available, the uncertainty of mass flow rate prediction from the current approach cannot be determined.

Figure 8 shows the experimental PCM-HX (left) and the control volume used to model its refrigerant side (right). The lengths of various geometrical parameters are given in Table 2. The PCM fills the empty space in the container. The control volume inlet and outlet are modeled using fluidports, while the heat transfer is modeled using the heatport connector. Since the control volume is lumped, the black dot at the center of Figure 8 (right) represents the location of the fluid element.

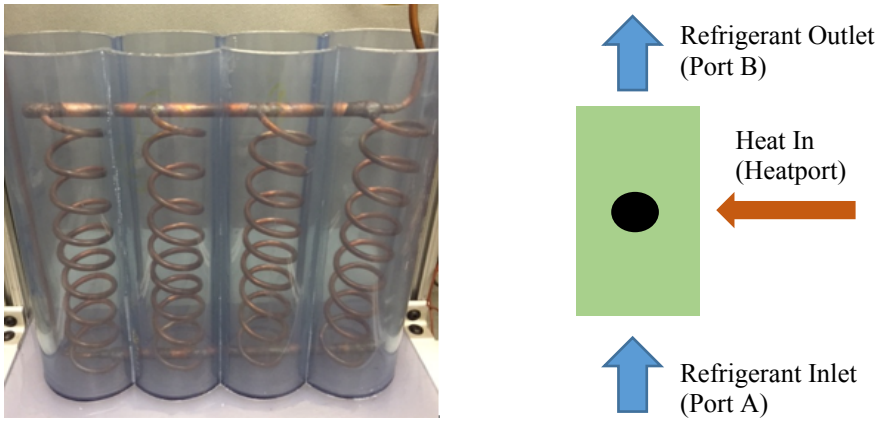

Figure 8: PCM-HX used in RoCo and the control volume used for modeling.

Table 2: Geometric parameters of PCMHX

Parameter	Value
Height between Headers [m]	0.315
Length of Header [m]	0.32
Diameter of helix turn [m]	0.41
Number of turns	9
Header tube outer diameter [m]	0.0127
Helix tube outer diameter [m]	0.00635

The total volume of the refrigerant tube (V_{tot}) consists of the volume occupied by the vapor (V_v) and the volume occupied by the liquid refrigerant (V_l). Out of the two properties required to determine the refrigerant state, the first (the average density, ρ_{cv}) can be calculated as follows:

$$V_{tot} = V_l + V_v \tag{20}$$

$$m = \rho_l V_l + \rho_v V_v \tag{21}$$

$$\frac{dm}{dt} = \dot{m}_{in} - \dot{m}_{out} \tag{22}$$

$$\rho_{cv} = \frac{m}{V_{tot}} \tag{23}$$

The second property (pressure, p_{cv}), can be obtained by averaging the pressure at the inlet and outlet as shown in Equation 24.

$$p_{cv} = \frac{p_{in} + p_{out}}{2} \tag{24}$$

These two properties are sufficient to determine the state of refrigerant, and all the remaining properties are calculated. Functions are available from the in-house REFPROP® 9.0 based library [54] for refrigerant media.

The energy conservation equation (Equation 25) and chain rule of derivatives applied to the partial derivative of density with state variables (Equation 26) are used to update pressure and specific enthalpy, which are the state variables. The partial derivatives of density are also functions of state variables [33] and evaluated using property functions [54].

$$V_{tot}\frac{dh_{cv}}{dt} + h\left(\dot{m}_{out} - \dot{m}_{in}\right) + \left(\dot{m}_{out}h_{out} - \dot{m}_{in}h_{in}\right) = \dot{Q}_r + V_{tot}\frac{dp_{cv}}{dt} \tag{25}$$

$$\frac{\partial \rho_{cv}}{\partial t} = \left.\frac{\partial \rho_{cv}}{\partial p_{cv}}\right|_{h_{cv}} \frac{dp_{cv}}{dt} + \left.\frac{\partial \rho_{cv}}{\partial h_{cv}}\right|_{P_{cv}} \frac{dh_{cv}}{dt} \tag{26}$$

$$\dot{Q}_{r,e} = \alpha_{r,e} A\left(T_{tube} - T_{cv}\right) \tag{27}$$

$$h_{out} = h_{v,cv} \tag{28}$$

$$h_{in} = h_{l,cv} \tag{29}$$

The heat transfer coefficient for heat transfer from the heatport, α_r in Equation 27, is calculated from Shah's correlation [64] with Schmidt correlation [65] for helical coils used for calculating liquid-only heat transfer coefficient. Since enthalpy in the fluidport is defined as a stream variable [66], outflow enthalpies need to be set for both the inlet and outlet. The outflow enthalpy at the outlet, h_{out}, is set as saturated vapor enthalpy, $h_{v,cv}$ in Equation 28, while the outflow enthalpy at the inlet port is set as saturated liquid enthalpy, $h_{l,cv}$ in Equation 29.

4. System Modeling

The nature of PCM-HX model used in the study is relatively simple to reduce the complexity of dynamics of thermosiphon assisted solidification for a system level simulation. To check the level of accuracy of the PCM-HX model for solidification, the experiment described in section 3.3.3 is simulated. The inlet water temperature from Figure 6 (left) and mass flow rate of water is given as input to predict the water outlet temperature. The model diagram for this simulation is shown in Figure 9.

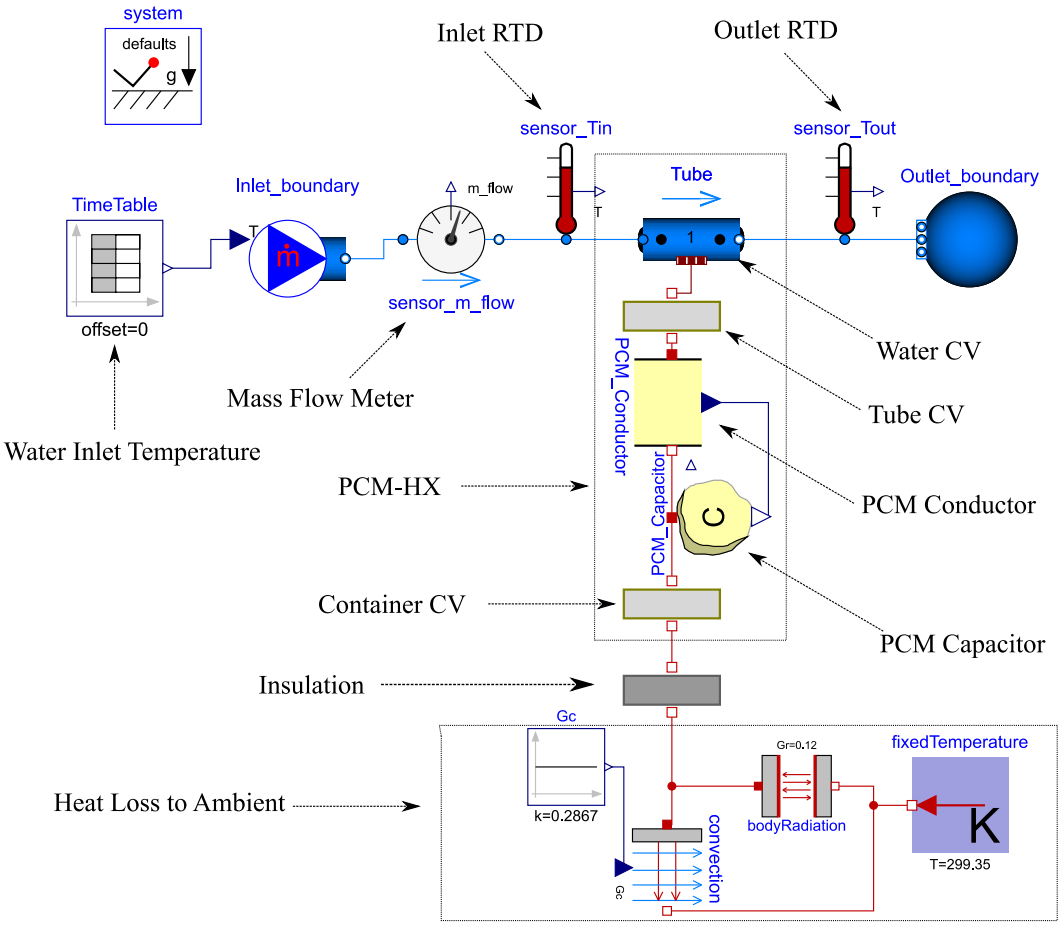

Figure 9: Model diagram for solidification experiment with water

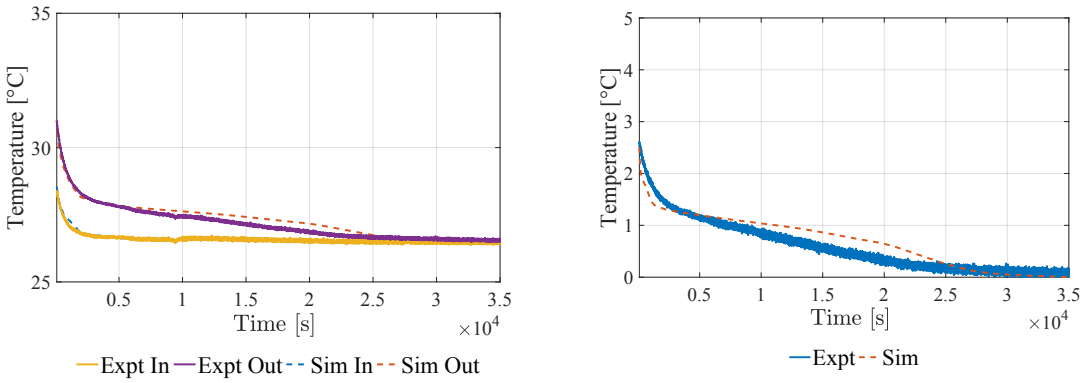

Figure 10: Water temperatures at the inlet and outlet of PCM-HX (left), Temperature difference between inlet and outlet of PCM-HX (right)

Error! Reference source not found. are shown in Figure 10, which compares the temperatures at the inlet and outlet of PCM-HX for the simulation the experimental data. The outlet temperature predicted is within 0.5°C of the experiment. The cumulative error from integrating the temperature difference over the entire time duration is 13.4%. Thus, the PCM-HX model is able to predict the solidification to a reasonable accuracy.

Figure 11 shows the model diagram for a thermosiphon using the components developed in the previous section. The experimental data for validation of the model is taken from Du et al.[31]. The refrigerant side two-phase heat transfer coefficient values of AC-HX (α_r in Equation 10) are calculated using Shah [67] correlation, and the heat transfer coefficients for the airside (α_a in Equations 11 and 12) are evaluated using Wang et al. [68] correlation.

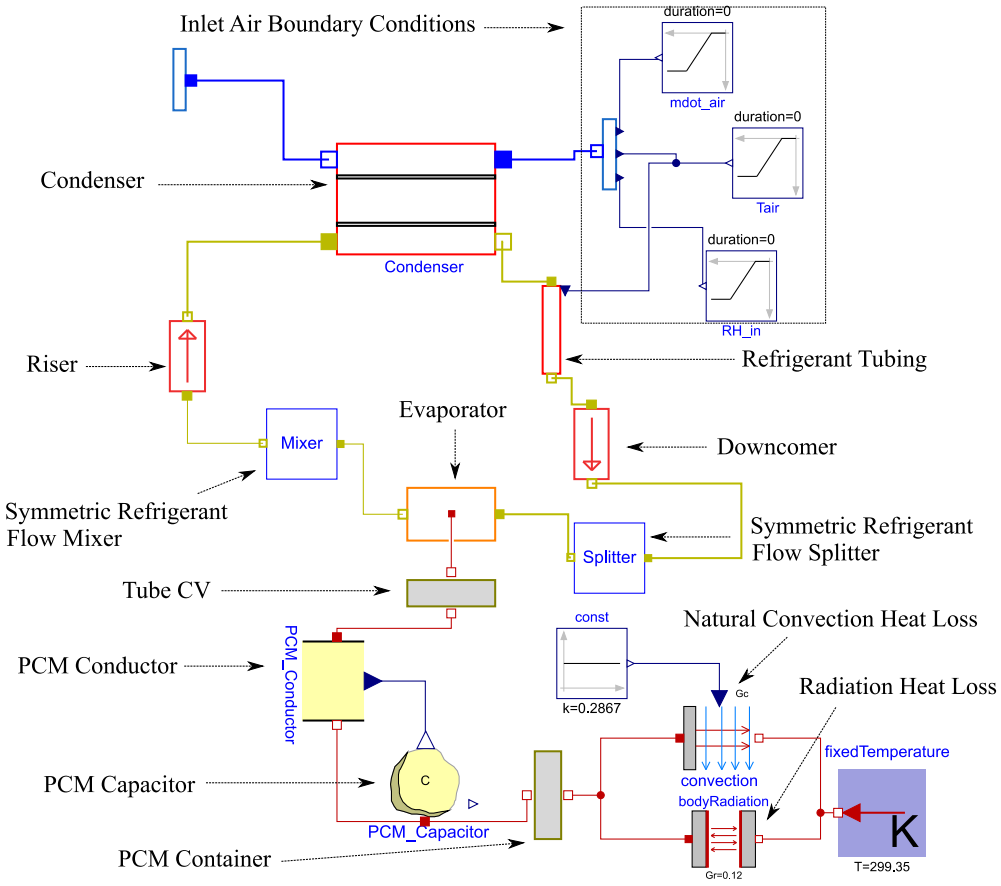

Figure 11: Modelica model used for the thermosiphon simulation with pure PCM.

Heat loss from the PCM Container to the surroundings by both natural convection and radiation is modeled. A tube element is used for modeling the PCM container, and thermophysical properties of PVC (density = 1300 kgm^{-3}, specific heat capacity = 900 $Jkg^{-1}K^{-1}$, thermal conductivity = 0.19 $Wm^{-1}K^{-1}$) are given as inputs. The heat transfer coefficient for natural convection from the PCM Container wall to the surroundings is calculated using Churchill-Chu correlation [69] for natural convection from vertical plates. For modeling radiation, it is assumed that the PCM Container is a small convex black-body in a large room.

The model is simulated using Radau IIa – order 5 stiff solver with a tolerance of 1e-06. Radau IIA is a single-step 3-stage implicit Runge-Kutta method. The details of various available solvers and comparison of their performance can be found in Liu et al. [70]. The experimental temperature of the PCM at the axis of the helical coil and at the wall (Figure 8 , left) is compared with the lumped CV temperature from the model in Figure 12 (left). T-Type thermocouples were used for the temperature measurement with the uncertainty of temperature measure of 0.5°C. The thermocouples were calibrated between 0-80°C with 10°C increments.

The PCM wall temperature refers to the temperature measured by the thermocouples between the PCM container wall and outside the helical coil. This is lower than the temperature in the axis region of the helical coils because the axis region gets heated from all sides, while the region outside the helical coil dissipates heat to the ambient. The thermocouple temperature falls faster than the simulation temperature because the thermocouples are located close to the helical coil, and they may not be exact representation of volume averaged temperature of the entire lump of PCM.

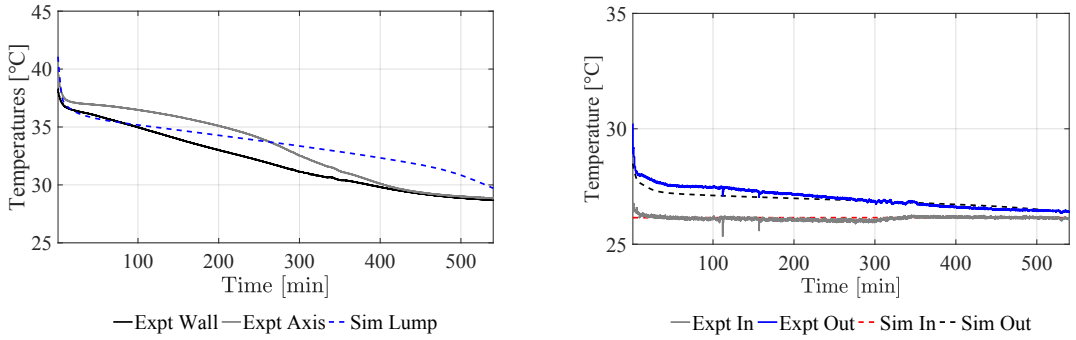

Figure 12: PCM temperature (Left) and Condenser airside temperature (right) comparison between experimental data [31] and simulation results

Figure 12 (right) shows the comparison of the condenser airside temperatures to the experimental data. Though there is a slight mismatch in the initial part of the cycle, which can be attributed to lack of a receiver model in the simulation model, the model can accurately predict the discharge time and can be used for the material selection study. Four T-Type thermocouples were installed each at the inlet and outlet of the condenser to measure the airside temperatures. Details of installation and uncertainty of the measurement are available in [71]. The heat losses from both convection and radiation to the surroundings contribute to 22% of heat losses. Thus, it is important to model these heat losses for accurate simulation of solidification.

5. Material Enhancement

Thermal conductivity enhancement of the PCM enables faster discharge than a pure PCM system. Compressed expanded natural graphite (CENG) foam is of interest due to the low density and high thermal conductivity of the material. Recall that the PCM Conductor component requires the heat transfer coefficient vs melt fraction as an input. The graphite enhanced PCM involves straight refrigerant tubes and has conduction dominant heat transfer [37], [72]. Consequently, the heat transfer coefficient for the composite

can be evaluated using the 2-D finite element model developed by Mallow et al. [38] and given as an input to PCM Conductor block. To eliminate the need to obtain DSC curves for each of the proposed materials, the effective heat capacity method is used for the conceptual evaluation of the PCM-HX performance with a CENG PCM composite. This method provides an enthalpy-temperature profile by taking specific heat capacities of solid and liquid phases and the temperature glide for phase change as inputs [60], [61], [73].

To model solidification in the CENG PCM composite, the average refrigerant temperature profile (Figure 13) from the experimental data [31] for pure PCM is used as an input. The heat transfer coefficient (α_{PCM}) is assumed to be independent of temperature in the small operating temperature range of the thermosiphon. This enables the use of the same boundary conditions for all of the finite element component simulations.

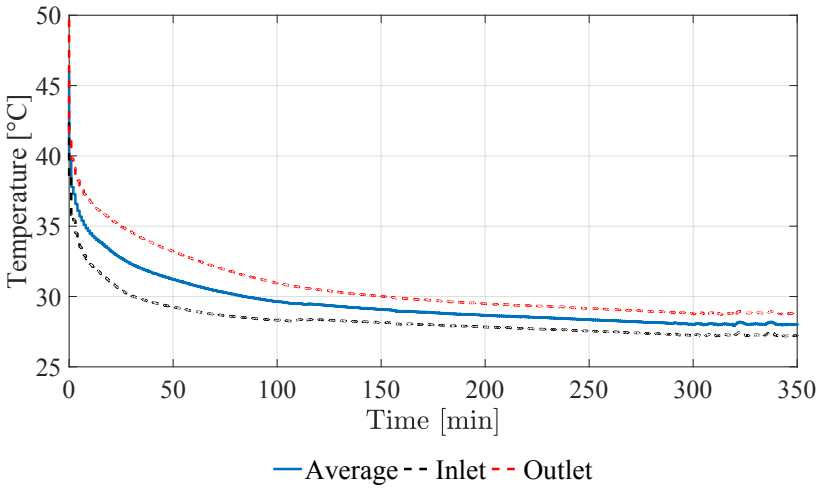

Figure 13: Refrigerant temperatures from pure PCM thermosiphon experiment.

To model CENG PCM composites of varying graphite densities, the thermophysical properties and geometry for each graphite density must be defined. The density and specific heat of the composite can be adjusted as a function of the CENG volume fraction (Equation 30), $\boldsymbol{\gamma}$, as shown in Equations 31 and 32[38]. The thermal conductivity is based on measurements reported in Mallow et al. [14]. As previously mentioned, the fabrication technique for CENG can result in closed pores that form voids of trapped air that are impenetrable by PCM. By studying the amount of PCM absorbed by the sample compared to the theoretical

maximum, Py et al. [35] found that the higher the volume fraction, the greater the volume of closed pores. This impacts all thermophysical properties, but has the greatest impact on the composite latent heat capacity. Therefore, in this work, two studies are completed. First, the maximum latent heat, adjusted by the graphite volume fraction as shown in Equation 33, is used for an ideal material. Second, the percent decrease in latent heat as a function of graphite volume fraction reported in [38] is used to represent a more practical system. As shown in Table 3, the main difference between these latent heat values is for the higher bulk densities when the volume of closed pores is greater.

$$\gamma = \frac{V_{CENG}}{V_{tot}} \tag{30}$$

$$\rho_{eff} = (1-\gamma)\rho_{PCM} + \gamma\rho_{gr} \tag{31}$$

$$c_{eff} = (1-\gamma)\frac{\rho_{PCM}}{\rho_{eff}}c_{PCM} + \gamma\frac{\rho_{gr}}{\rho_{eff}}c_{gr} \tag{32}$$

$$h_{sl,ideal} = (1-\gamma)\frac{\rho_{PCM}}{\rho_{eff}}h_{sl,PCM} \tag{33}$$

Table 3: Properties of PCM and PCM composites.

CENG Bulk Density (kgm^{-3})	CENG Volume Fraction	Density (kgm^{-3})		Specific Heat ($Jkg^{-1}K^{-1}$)		Latent Heat Ideal (Jg^{-1})	Latent Heat Measured (Jg^{-1})	Thermal Conductivity ($Wm^{-1}K^{-1}$)
		Solid	Liquid	Solid	Liquid			
0	0.0%	920	840	2210	2630	210	210	0.25 (s); 0.15 (l)
11	0.5%	927	847	2192	2605	208	208	1.1
23	1.0%	934	854	2173	2578	205	205	2.3
50	2.2%	950	871	2131	2520	200	200	4.7
100	4.4%	979	903	2057	2417	187	176	9.6
143	6.3%	1005	930	1997	2335	178	145	20.2

The geometry used for all simulations is shown in Figure 15. A standard copper tube (outer diameter (OD) = 0.25 in), PCM composite, and outer plastic shell (thickness = 5 mm) is shown in Figure 15. While typical copper and plastic properties were used for all simulations, the properties for the CENG PCM composite were adjusted as a function of CENG volume fraction as listed in Table 3. To maintain the same thermal storage capacity for each simulation, the composite OD was adjusted to account for the changes in the latent heat. A practical OD value of 75 mm was used for the lowest graphite volume fraction and then

adjusted for each subsequent system based on the composite specific and latent heat reported in Table 3. The composite OD for each system is listed in Table 4**.**

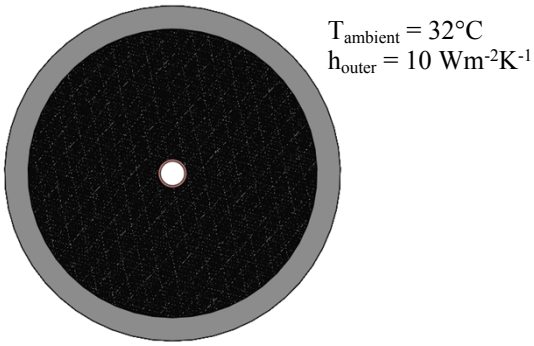

Figure 14: Cross section of the PCM-HX profile used for 2D finite element simulation.

Table 4: Geometry adjusted for composite energy density.

CENG Bulk Density (kgm^{-3})	CENG Volume Fraction	PCM OD Ideal (mm)	PCM OD Measured (mm)
11	0.5%	75.0	75.0
23	1.0%	75.4	75.4
50	2.2%	76.1	76.1
100	4.4%	77.4	81.1
143	6.3%	78.7	91.9

The effects of both natural convection and radiation on the outer wall of the PCM container are accounted for by providing an outer wall heat transfer coefficient of 10 $Wm^{-2}K^{-1}$. The mid-point of the liquid to solid phase change temperature range was 35°C with a temperature glide of 2°C. The initial temperature of the CENG PCM composite is set to the initial temperature of the refrigerant. The average transient refrigerant temperature profile shown in Figure 13 is applied to the inner surface of the copper tube. Negligible contact resistance between the tube and CENG PCM composite was assumed for the ideal case. For the case with measured properties, a 50 μm gap between the tube and the composite was added. This gap represents the space required to accommodate insertion of the refrigerant tube, which fills with wax following the first melt due to wax expansion based on prior experimental results.

To calculate the average heat transfer coefficient for each CENG volume fraction, the transient heat flux at the refrigerant tube was divided by the difference between the outer refrigerant tube temperature and the temperature at the PCM outer diameter. This value was averaged for the entire simulation and is graphed in

Figure 15 for both the ideal case and the practical case. These heat transfer coefficients were then incorporated in the system level modeling.

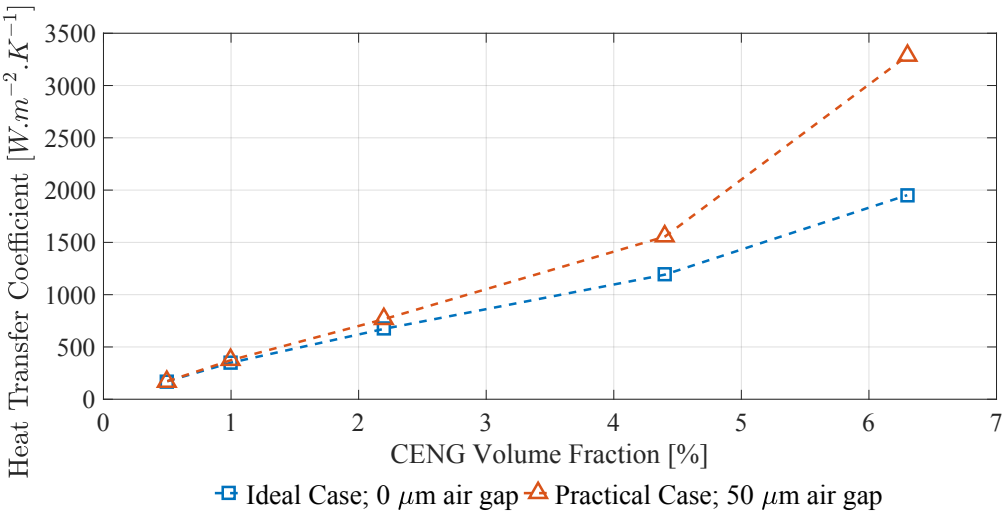

Figure 15: Average heat transfer coefficient as a function of CENG volume fraction.

6. System Modeling for CENG PCM

The inlet air temperature for discharge operation is 79°F (26.15°C). The thermal storage consists of four PCM cylinders with a height of 1.2 m. The outer diameters of these cylinders are given in Table 4. The air flow rate of the fan blowing on the AC-HX is 80 cfm (0.038 m^3/s).

The thermosiphon model is similar to the one shown in Figure 11 with just one modification: the solidification behavior is modeled by the effective heat capacity method[74]. The discharge time for the pure PCM is calculated from the pure PCM simulation to be 554 minutes with the final 10% taking up 114 minutes. For good cyclic efficiency, it does not make sense to solidify the material to 0% liquid, and so the discharge time for the baseline case is taken to be 440 minutes. Koz et al. [75] reached a similar conclusion that it is not worthwhile to completely melt the thermal storage for a cyclic operation. Consequently, due to the poor thermal conductivity of pure PCM, the thermal storage needs to be slightly oversized since the PCM residing at further ends of the storage from the heat source or sink are difficult to melt or solidify.

A scaled-down version of thermal storage is first developed from a graphite enhanced material and validated with the water based solidification similar to the one described in section 3.3.3 to obtain a good

match. Simulations are carried out for all the materials listed in Table 3. The heat transfer area between the PCM and refrigerant tube is kept the same in all simulations. The liquid-only value from Dittus Boelter [76] correlation is used as input to the Shah correlation [64] for two-phase heat transfer coefficient evaluation with straight tubes. The surface area for the heat loss changes due to the difference in the volume of each CENG PCM required to provide the same thermal storage capacity. Discharge time, weight, and volume are normalized to that of RoCo (440 minutes) and plotted in Figure 16 using the heat transfer coefficients for the practical case shown in Figure 15.

It can be observed that increased graphite density reduces the discharge time of the PCM-HX. The decrease in discharge time is sharp until 2.2% CENG volume fraction. For the denser materials, the heat transfer coefficient on the refrigerant side is lower than the heat transfer coefficient of the melting PCM and becomes the limiting factor. Another interesting observation is that, in spite of 5 times increase in thermal conductivity in comparison to the pure PCM, the composite with 0.5% CENG PCM does not provide significant improvement to the discharge time. This can be attributed to two factors: lack of natural convection based circulation in the PCM due to the graphite foam and reduced refrigerant-side heat transfer coefficient from the use of straight tubes instead of helical tubes for the pure PCM.

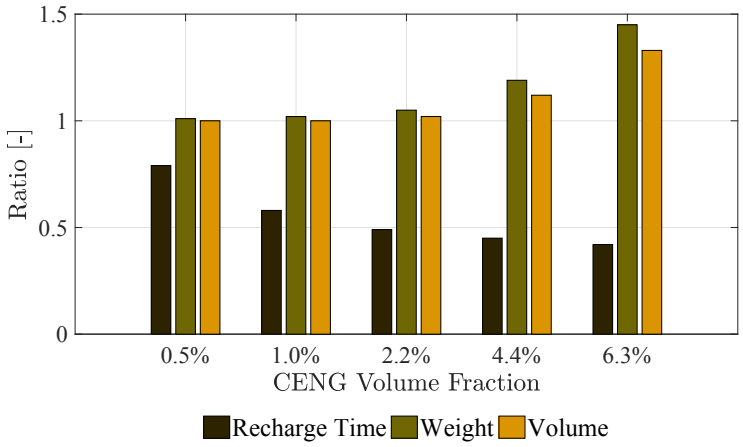

Figure 16: Relative performance of various CENG composites capable of a two-hour operation time.

The temperature profile of the PCM for the CENG PCM is plotted in Figure 17 (left). The initial sharp drop in temperature corresponds to sensible heat in the liquid phase. The amount of heat stored as sensible

heat is much lesser than the latent heat and is easily released. The next portion corresponds to latent heat while the PCM solidifies from liquid to solid. The slope increases with the increased amount of graphite in CENG. Finally, the sharp drop corresponds to sensible heat in the solid phase of the PCM. As the PCM reaches the ambient temperature, the heat release rate decreases and so the temperature of PCM approaches the ambient temperature asymptotically.

Figure 17 (right) shows the different rate of heat release from the PCM. As expected, the higher graphite content leads to increased heat release rate. This leads to the faster recharge time since the net heat stored is the same for all the thermal storages. The temperature profiles are much different than the pure PCM case shown in Figure 12 (left). This can be attributed to the lack of natural convection in CENG. The graphite foam blocks passages for liquid PCM to develop convection current. Additionally, the higher thermal conductivity reduces the temperature gradient that drives natural convection.

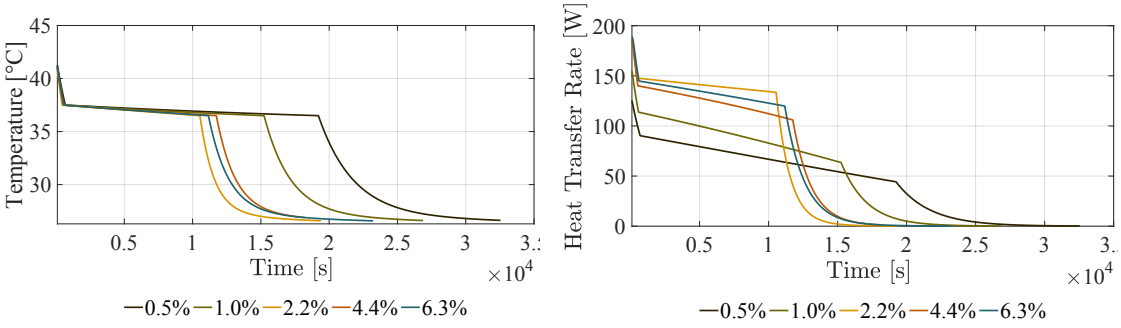

Figure 17: Temperature profile (left) and heat removal rate (right) during thermosiphon operation with enhanced graphite thermal storage

7. Discussion

The results obtained in the previous section suggest that there is a significant reduction in the discharge time if the thermal storage is made from CENG. The thermosiphon operation requires continuous operation of a 10-W fan for the duration of the discharge process. Thus, shortening the process results in an increased coefficient of performance (COP) for the operation. Du et al. [31] reported the COP of the VCC equal to 2.85. The system COP for RoCo should incorporate the power consumed during both the cooling as well as the recharge process.

For the present analysis, the COP for the VCC will be assumed constant for all the variations of thermal storage. In reality, the CENG thermal storage will have lower condenser temperature due to improved thermal conductivity and will further enhance the COP. The evaporator capacity reported by Du et al. [31] is 165.6 W for a period of two hours. This value is averaged value over the two hour period. Average power consumption for the two-hour interval can be calculated from Equation 32 = 58.1 W.

$$COP_{vcc} = \frac{\bar{Q}}{\bar{W}_{vcc}} \tag{32}$$

$$COP_{tot} = \frac{\bar{Q}\left(\Delta t_{vcc}\right)}{\bar{W}_{vcc}\left(\Delta t_{vcc}\right) + \bar{W}_{ts}\left(\Delta t_{ts}\right)} \tag{33}$$

Equation 33 can be used to evaluate the overall COP for RoCo. This incorporates the energy consumed during both recharge and discharge processes. The results for all the cases are presented in Figure 14. It can be observed that the COP is in the range of 1.75 to 2.25 for all the PCM composites. The COP can be increased by as high as 29% for the CENG with the volume fraction of 6.3%.

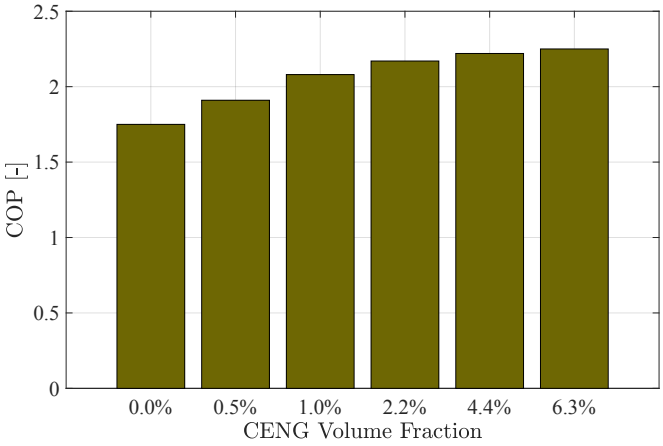

Figure 18: COP of RoCo for the different thermal storage options

The payback period for RoCo is estimated to be in the range of 5-10 years [22]. However, the selling price of a single device for mass production is of the order of a few hundred dollars[22]. Heidarinejad et al. [23] found that the technology is more suitable for midrise apartments than office buildings during a cooling season. The cash savings per person for midrise apartments for Honolulu, New York City and Phoenix were calculated to be $62/year, $40/year and $37/year, respectively[23]. The use of extended set-point

temperatures could reduce CO_2 emissions up to 21.4% per year[23]. The elevation of cooling setpoint of the building HVAC by at least 4°F (2.2°C) is expected to provide energy savings in the range of 10-30%[32].

Future investigations will involve experimental investigations of designs with graphite enhanced designs. Recharge time may also be increased by using a PCM which solidifies at a higher temperature. This will provide a larger potential for the temperature gradient to solidify the PCM at a faster rate. Increasing the phase change temperature of thermal storage will, however, decrease the COP of VCC operation. Dynamic simulations of both VCC and thermosiphon will be used to find the appropriate set of phase change material and enhancement options for a longer cooling operation for RoCo.

8. Conclusions

An innovative portable air conditioning system called RoCo is introduced, which relies on melting and solidifying a PCM inserted in a heat exchanger for efficient operation. RoCo uses a thermosiphon for recharging the PCM. The paraffin-based PCM thermal storage unit needed about eight hours for solidification after a two-hour cooling operation. This limits the cooling operation time of RoCo to a single cycle per day. A transient model for the thermosiphon process is developed to understand the process and explore the thermal storage performance of graphite enhanced PCM. Equations for modeling the PCM, riser, downcomer, and evaporator are discussed in detail. An empirical heat transfer coefficient equation for solidification of PCM by helical coil is derived via experiments. The simulation is validated with experimental data from an earlier study. The validated thermosiphon model is then used to predict the system behavior with PCM composite materials of varying graphite density. Based on this work, the 2.2% graphite volume fraction composite is considered the most promising due to the 51% reduction in the discharge time paired with a 5% increase in weight. The coefficient of performance for overall operation is increased by 24%. The graphite enhanced version shows promising results and will be investigated in future prototypes. Deployment of RoCo can lead to potential savings of energy, cost and CO_2 emissions.

Nomenclature

A	area [m^2]
c	specific heat capacity [J kg^{-1} K^{-1}]
COP	coefficient of performance [-]
d	diameter [m]
f	friction factor [-]
g	acceleration of gravity [m s^{-2}]
h	specific enthalpy [J kg^{-1} K^{-1}]
h_{fg}	enthalpy of fusion [J kg^{-1}]
L	length [m]
Le	Lewis number [-]
k	thermal conductivity [$Wm^{-1}K^{-1}$]
m	mass [kg]
$\dot{m}$	mass flow rate [kg s^{-1}]
p	pressure [Pa]
$\dot{Q}$	heat transfer rate [W]
Re	Reynolds number [-]
S	perimeter [m]
t	time [s]
T	temperature [K]
u	velocity [m s^{-1}]
V	volume [m^3]
W	Power consumed [W]
z	height [m]

Greek Symbols

$\propto$	heat transfer coefficient [$Wm^{-2}K^{-1}$]
λ	melt fraction [-]
ρ	density [kg m^{-3}]
γ	volume fraction [-]
ω	humidity ratio [-]

Subscripts

a	moist air
avg	average
cv	control volume
e	evaporator
eff	effective
gr	graphite
in	inlet
l	liquid
out	outlet
pcm	phase change material
r	refrigerant
s	solid
tot	total
$tube$	refrigerant tube
ts	thermosiphon
v	vapor
vcc	vapor compression cycle

Acknowledgements

This research was supported by the Advanced Research Projects Agency - Energy (ARPA-E) with Award Number DE-AR0000530. We thank the members of Center for Environmental Energy Engineering (CEEE), Oak Ridge National Laboratory (ORNL), and team members of the Roving Comforter Project for their support.

References

[1] United States Department of Energy, *Buildings Energy Data Book*. 2011.

[2] A. Makhoul, K. Ghali, and N. Ghaddar, "Thermal comfort and energy performance of a low-mixing ceiling-mounted personalized ventilator system," *Build. Environ.*, vol. 60, pp. 126–136, 2013.

[3] M. Kong, T. Q. Dang, J. Zhang, and H. E. Khalifa, "Micro-environmental control for efficient local cooling," *Build. Environ.*, vol. 118, pp. 300–312, 2017.

[4] Y. Chen, B. Raphael, and S. C. Sekhar, "Individual control of a personalized ventilation system integrated with an ambient mixing ventilation system," *HVAC&R Res.*, vol. 18, no. 6, pp. 1136–1152, 2012.

[5] S. Watanabe, A. K. Melikov, and G. L. Knudsen, "Design of an individually controlled system for an optimal thermal microenvironment," *Build. Environ.*, vol. 45, no. 3, pp. 549–558, 2010.

[6] J. Kaczmarczyk, A. Melikov, Z. Bolashikov, L. Nikolaev, and P. O. Fanger, "Human Response to Five Designs of Personalized Ventilation," *HVAC&R Res.*, vol. 12, no. 2, pp. 367–384, 2006.

[7] N. Mao, D. Pan, Z. Li, Y. Xu, M. Song, and S. Deng, "A numerical study on influences of building envelope heat gain on operating performances of a bed-based task/ambient air conditioning (TAC) system in energy saving and thermal comfort," *Appl. Energy*, vol. 192, pp. 213–221, 2017.

[8] H. Zhang *et al.*, "Using footwarmers in offices for thermal comfort and energy savings," *Energy Build.*, vol. 104, pp. 233–243, 2015.

[9] H. Oi, K. Yanagi, K. Tabata, and Y. Tochihara, "Effects of heated seat and foot heater on thermal comfort and heater energy consumption in vehicle," *Ergonomics*, vol. 54, no. 8, pp. 690–699, 2011.

[10] Y. He, N. Li, M. He, and D. He, "Using radiant cooling desk for maintaining comfort in hot environment," *Energy Build.*, vol. 145, pp. 144–154, 2017.

[11] W. Pasut, H. Zhang, E. Arens, and Y. Zhai, "Energy-efficient comfort with a heated/cooled chair: Results from human subject tests," *Build. Environ.*, vol. 84, pp. 10–21, 2015.

[12] J. Niu, N. Gao, M. Phoebe, and Z. Huigang, "Experimental study on a chair-based personalized ventilation system," *Build. Environ.*, vol. 42, no. 2, pp. 913–925, 2007.

[13] S. Watanabe, T. Shimomura, and H. Miyazaki, "Thermal evaluation of a chair with fans as an individually controlled system," *Build. Environ.*, vol. 44, no. 7, pp. 1392–1398, 2009.

[14] H. Cao, D. H. Branson, S. Peksoz, J. Nam, and C. A. Farr, “Fabric Selection for a Liquid Cooling Garment,” *Text. Res. J.*, vol. 76, no. 7, pp. 587–595, 2006.

[15] A. D. Flouris and S. S. Cheung, “Design and control optimization of microclimate liquid cooling systems underneath protective clothing,” *Ann. Biomed. Eng.*, vol. 34, no. 3, pp. 359–372, 2006.

[16] H. Hamdan, N. Ghaddar, D. Ouahrani, K. Ghali, and M. Itani, “PCM cooling vest for improving thermal comfort in hot environment,” *Int. J. Therm. Sci.*, vol. 102, pp. 154–167, 2016.

[17] W. Song, F. Wang, and F. Wei, “Hybrid cooling clothing to improve thermal comfort of office workers in a hot indoor environment,” *Build. Environ.*, vol. 100, pp. 92–101, 2016.

[18] Y. J. Dai and K. Sumathy, “Theoretical study on a cross-flow direct evaporative cooler using honeycomb paper as packing material,” *Appl. Therm. Eng.*, vol. 22, no. 13, pp. 1417–1430, 2002.

[19] F. J. R. Martínez, E. V. Gómez, R. H. Martín, J. M. Gutiérrez, and F. V. Diez, “Comparative study of two different evaporative systems: An indirect evaporative cooler and a semi-indirect ceramic evaporative cooler,” *Energy Build.*, vol. 36, no. 7, pp. 696–708, 2004.

[20] J. R. Camargo, C. D. Ebinuma, and J. L. Silveira, “Experimental performance of a direct evaporative cooler operating during summer in a Brazilian city,” *Int. J. Refrig.*, vol. 28, no. 7, pp. 1124–1132, 2005.

[21] W. Chakroun, N. Ghaddar, and K. Ghali, “Chilled ceiling and displacement ventilation aided with personalized evaporative cooler,” *Energy Build.*, vol. 43, no. 11, pp. 3250–3257, 2011.

[22] R. Dhumane, J. Ling, V. Aute, and R. Radermacher, “Portable personal conditioning systems : Transient modeling and system analysis,” *Appl. Energy*.

[23] M. Heidarinejad, D. A. Dalgo, N. W. Mattise, and J. Srebric, “Personalized cooling as an energy efficiency technology for city energy footprint reduction,” *J. Clean. Prod.*, vol. 171, pp. 491–505, 2018.

[24] S. Zhu, D. Dalgo, J. Srebric, and S. Kato, “Cooling efficiency of a spot-type personalized air-conditioner,” *Build. Environ.*, vol. 121, pp. 35–48, 2017.

[25] R. Khodabandeh, “Heat transfer in the evaporator of an advanced two-phase thermosyphon loop,” *Int. J. Refrig.*, vol. 28, no. 2, pp. 190–202, 2005.

[26] N. Z. Aung and S. Li, “Numerical investigation on effect of riser diameter and inclination on system parameters in a two-phase closed loop thermosyphon solar water heater,” *Energy Convers. Manag.*, vol. 75, pp. 25–35, 2013.

[27] T. Yilmaz, “Computer simulation of two-phase flow thermosyphon solar water heating system,” *Energy Convers. Manag.*, vol. 32, no. 2, pp. 133–144, 1991.

[28] A. Chehade, H. Louahlia-Gualous, S. Le Masson, and E. Lépinasse, “Experimental investigations and modeling of a loop thermosyphon for cooling with zero electrical consumption,” *Appl. Therm. Eng.*, vol. 87, pp. 559–573, 2015.

[29] A. Samba, H. Louahlia-Gualous, S. Le Masson, and D. Nörterhäuser, “Two-phase thermosyphon loop for cooling outdoor telecommunication equipments,” *Appl. Therm. Eng.*, vol. 50, no. 1, pp. 1351–1360, 2013.

[30] H. Zhang, Z. Shi, K. Liu, S. Shao, T. Jin, and C. Tian, “Experimental and numerical investigation

on a CO 2 loop thermosyphon for free cooling of data centers," *Appl. Therm. Eng.*, vol. 111, pp. 1083–1090, 2017.

[31] Y. Du, J. Muehlbauer, J. Ling, V. Aute, Y. Hwang, and R. Radermacher, "Rechargeable Personal Air Conditioning Device," in *ASME 2016 10th International Conference on Energy Sustainability collocated with the ASME 2016 Power Conference and the ASME 2016 14th International Conference on Fuel Cell Science, Engineering and Technology*, 2016.

[32] T. Hoyt, E. Arens, and H. Zhang, "Extending air temperature setpoints: Simulated energy savings and design considerations for new and retrofit buildings," *Build. Environ.*, vol. 88, pp. 89–96, 2015.

[33] "Entropy Solutions LLC." [Online]. Available: http://www.puretemp.com/. [Accessed: 19-Oct-2017].

[34] D. A. Didion and G. E. Kelly, "New testing and rating procedures for seasonal performance of heat pumps," *ASHRAE J.*, vol. 21, no. 9, pp. 40–44, 1979.

[35] X. Py, R. Olives, and S. Mauran, "Paraffin/porous-graphite-matrix composite as a high and constant power thermal storage material," *Int. J. Heat Mass Transf.*, vol. 44, no. 14, pp. 2727–2737, 2001.

[36] Y. Zhong *et al.*, "Heat transfer enhancement of paraffin wax using compressed expanded natural graphite for thermal energy storage," *Carbon N. Y.*, vol. 48, no. 1, pp. 300–304, 2010.

[37] X. Wang, Q. Guo, Y. Zhong, X. Wei, and L. Liu, "Heat transfer enhancement of neopentyl glycol using compressed expanded natural graphite for thermal energy storage," *Renew. energy*, vol. 51, pp. 241–246, 2013.

[38] A. M. Mallow, O. Abdelaziz, and S. Graham, "Thermal Charging Study of Compressed Expanded Natural Graphite/Phase Change Material Composites," Oak Ridge National Laboratory (ORNL), Oak Ridge, TN (United States). Building Technologies Research and Integration Center (BTRIC), 2016.

[39] F. Dobran, "Steady-state characteristics and stability thresholds of a closed two-phase thermosyphon," *Int. J. Heat Mass Transf.*, vol. 28, no. 5, pp. 949–957, 1985.

[40] J. G. Reed and C. L. Tien, "Modeling of the two-phase closed thermosyphon," *J. Heat Transfer*, vol. 109, no. 3, pp. 722–730, 1987.

[41] S. Lips, V. Sartre, F. Lefevre, S. Khandekar, and J. Bonjour, "Overview of Heat Pipe Studies during the period 2010-2015," *Interfacial Phenom. Heat Transf.*, vol. 4, no. 1, 2016.

[42] A. Faghri, "Review and advances in heat pipe science and technology," *J. Heat Transfer*, vol. 134, no. 12, p. 123001, 2012.

[43] S. Riffat and X. Ma, "Recent developments in heat pipe technology and applications: a review," *Int. J. Low-Carbon Technol.*, vol. 2, no. 2, pp. 162–177, 2007.

[44] C. C. J. Vincent and J. B. W. Kok, "Investigation of the overall transient performance of the industrial two-phase closed loop thermosyphon," *Int. J. Heat Mass Transf.*, vol. 35, no. 6, pp. 1419–1426, 1992.

[45] S. I. Haider, Y. K. Joshi, and W. Nakayama, "A natural circulation model of the closed loop, two-phase thermosyphon for electronics cooling," *J. Heat Transfer*, vol. 124, no. 5, pp. 881–890, 2002.

[46] R. Khodabandeh, “Pressure drop in riser and evaporator in an advanced two-phase thermosyphon loop,” *Int. J. Refrig.*, vol. 28, no. 5, pp. 725–734, 2005.

[47] P. Zhang, B. Wang, W. Shi, L. Han, and X. Li, “Modeling and performance analysis of a two-phase thermosyphon loop with partially/fully liquid-filled downcomer,” *Int. J. Refrig.*, vol. 58, pp. 172–185, 2015.

[48] S. A. Klein and F. L. Alvarado, “Engineering equation solver,” *F-Chart Software, Madison, WI*, vol. 1, 2002.

[49] MATLAB User’s Guide, “The mathworks.” Natick, MA, 1993.

[50] R. T. Dobson and J. C. Ruppersberg, “Flow and heat transfer in a closed loop thermosyphon. Part I—Theoretical simulation,” *J. Energy South. Afr*, vol. 18, pp. 32–40, 2007.

[51] S. Bodjona, E. Videcoq, R. Saurel, A. Chinnayya, A. M. Benselama, and Y. Bertin, “Transient simulation of a two-phase loop thermosyphon with a model out of thermodynamic equilibrium,” *Int. J. Heat Mass Transf.*, vol. 108, pp. 2321–2332, 2017.

[52] R. Srikanth, R. S. Nair, and C. Balaji, “Thermosyphon assisted melting of PCM inside a rectangular enclosure: A synergistic numerical approach,” in *Journal of Physics: Conference Series*, 2016, vol. 745, no. 3, p. 32130.

[53] S. E. Mattsson, H. Elmqvist, and M. Otter, “Physical system modeling with Modelica,” *Control Eng. Pract.*, vol. 6, no. 4, pp. 501–510, 1998.

[54] V. Aute and R. Radermacher, “Standardized polynomials for fast evaluation of refrigerant thermophysical properties,” in *15th International Refrigeration and Air Conditioning Conference*, 2014, p. 2462:1-10.

[55] H. Elmqvist, H. Tummescheit, and M. Otter, “Object-oriented modeling of thermo-fluid systems,” in *3rd International Modelica Conference*, 2003, pp. 269–286.

[56] F. P. Incropera and D. P. Dewitt, “Introduction to Heat Transfer. 2002.” John Wiley and Sons, Chichester, New York.

[57] H. Qiao, V. Aute, and R. Radermacher, “Transient modeling of a flash tank vapor injection heat pump system–part I: model development,” *Int. J. Refrig.*, vol. 49, pp. 169–182, 2015.

[58] K. T. Hong and R. L. Webb, “Calculation of fin efficiency for wet and dry fins,” *HVAC&R Res.*, vol. 2, no. 1, pp. 27–41, 1996.

[59] H. Hu and S. A. Argyropoulos, “Mathematical modelling of solidification and melting: a review,” *Model. Simul. Mater. Sci. Eng.*, vol. 4, no. 4, p. 371, 1996.

[60] Y. Dutil, D. R. Rousse, N. Ben Salah, S. Lassue, and L. Zalewski, “A review on phase-change materials: Mathematical modeling and simulations,” *Renew. Sustain. Energy Rev.*, vol. 15, no. 1, pp. 112–130, 2011.

[61] M. Iten and S. Liu, “A work procedure of utilising PCMs as thermal storage systems based on air-TES systems,” *Energy Convers. Manag.*, vol. 77, pp. 608–627, 2014.

[62] V. R. Voller, “Fast implicit finite-difference method for the analysis of phase change problems,” *Numer. Heat Transf.*, vol. 17, no. 2, pp. 155–169, 1990.

[63] K. Merlin, D. Delaunay, J. Soto, and L. Traonvouez, “Heat transfer enhancement in latent heat thermal storage systems: comparative study of different solutions and thermal contact investigation between the exchanger and the PCM,” *Appl. Energy*, vol. 166, pp. 107–116, 2016.

[64] M. M. Shah, “Chart correlation for saturated boiling heat transfer: equations and further study,” *ASHRAE Trans.;(United States)*, vol. 88, no. CONF-820112-, 1982.

[65] E. F. Schmidt, “Wärmeübergang und druckverlust in rohrschlangen,” *Chemie Ing. Tech.*, vol. 39, no. 13, pp. 781–789, 1967.

[66] R. Franke *et al.*, “Stream connectors-an extension of Modelica for device-oriented modeling of convective transport phenomena,” in *Proceedings of the 7th International Modelica Conference; Como; Italy; 20-22 September 2009*, 2009, no. 43, pp. 108–121.

[67] M. M. Shah, “Comprehensive correlations for heat transfer during condensation in conventional and mini/micro channels in all orientations,” *Int. J. Refrig.*, vol. 67, pp. 22–41, 2016.

[68] C.-C. Wang, K.-Y. Chi, and C.-J. Chang, “Heat transfer and friction characteristics of plain fin-and-tube heat exchangers, part II: Correlation,” *Int. J. Heat Mass Transf.*, vol. 43, no. 15, pp. 2693–2700, 2000.

[69] S. W. Churchill and H. H. S. Chu, “Correlating equations for laminar and turbulent free convection from a vertical plate,” *Int. J. Heat Mass Transf.*, vol. 18, no. 11, pp. 1323–1329, 1975.

[70] L. Liu, F. Felgner, and G. Frey, “Comparison of 4 numerical solvers for stiff and hybrid systems simulation,” in *Emerging Technologies and Factory Automation (ETFA), 2010 IEEE Conference on*, 2010, pp. 1–8.

[71] Y. Du, “Battery powered portable vapor compression cycle system with PCM condenser.” 2016.

[72] M. M. Sedeh and J. M. Khodadadi, “Thermal conductivity improvement of phase change materials/graphite foam composites,” *Carbon N. Y.*, vol. 60, pp. 117–128, 2013.

[73] P. Lamberg, R. Lehtiniemi, and A.-M. Henell, “Numerical and experimental investigation of melting and freezing processes in phase change material storage,” *Int. J. Therm. Sci.*, vol. 43, no. 3, pp. 277–287, 2004.

[74] Y. Cao and A. Faghri, “A numerical analysis of phase-change problems including natural convection,” *J. Heat Transfer*, vol. 112, no. 3, pp. 812–816, 1990.

[75] M. Koz, H. S. Erden, and H. E. Khalifa, “Numerical Investigation of the Melting of a Phase Change Material in a Thermal Storage Device With Embedded Air Flow Channels,” in *ASME. Heat Transfer Summer Conference*, 2016, no. 50336, p. V002T08A022.

[76] F. W. Dittus and L. M. K. Boelter, “Heat transfer in automobile radiators of the tubular type,” *Int. Commun. Heat Mass Transf.*, vol. 12, no. 1, pp. 3–22, 1985.